

POINT-SPREAD FUNCTIONS FOR THE EXTREME-ULTRAVIOLET CHANNELS OF *SDO*/AIA TELESCOPES

B. PODUVAL¹, C. E. DEFOREST¹, J. T. SCHMELZ², AND S. PATHAK²

¹ Southwest Research Institute, 1050 Walnut Street, Suite 300, Boulder, CO 80302, USA; bala@boulder.swri.edu

² Physics Department, University of Memphis, Memphis, TN 38152, USA

Received 2012 October 26; accepted 2013 January 15; published 2013 February 27

ABSTRACT

We present the stray-light point-spread functions (PSFs) and their inverses we characterized for the Atmospheric Imaging Assembly (AIA) EUV telescopes on board the *Solar Dynamics Observatory* (*SDO*) spacecraft. The inverse kernels are approximate inverses under convolution. Convolution of the original Level 1 images with them produces images with improved stray-light characteristics. We demonstrate the usefulness of these PSFs by applying them to two specific cases: photometry and differential emission measure (DEM) analysis. The PSFs consist of a narrow Gaussian core, a diffraction component, and a diffuse component represented by the sum of a Gaussian-truncated Lorentzian and a *shoulder* Gaussian. We determined the diffraction term using the measured geometry of the diffraction pattern identified in flare images and the theoretically computed intensities of the principal maxima of the first few diffraction orders. To determine the diffuse component, we fitted its parameterized model using iterative forward-modeling of the lunar interior in the *SDO*/AIA images from the 2011 March 4 lunar transit. We find that deconvolution significantly improves the contrast in dark features such as miniature coronal holes, though the effect was marginal in bright features. On a percentage-scattering basis, the PSFs for *SDO*/AIA are better by a factor of two than that of the EUV telescope on board the *Transition Region And Coronal Explorer* mission. A preliminary analysis suggests that deconvolution alone does not affect DEM analysis of small coronal loop segments with suitable background subtraction. We include the derived PSFs and their inverses as supplementary digital materials.

Key words: instrumentation: miscellaneous – Sun: corona – Sun: UV radiation – techniques: image processing – telescopes

Online-only material: color figures, Supplemental data (FITS) file (tar.gz)

1. INTRODUCTION

An ideal imaging telescope would be a perfect detector of radiance versus direction within its passband, but real solar telescopes are far from perfect. Even after accounting for flat-field effects within the detector, telescope images exhibit convolution with a point-spread function (PSF) that describes the response of the system to a point source at infinity. To the first order, the stray-light PSF is independent of position in the focal plane and combines several effects: diffraction effects due to the quantum/wave dual nature of light, surface effects due to roughness, and other non-ideal properties of the telescope. These effects spread light, which would otherwise be destined for a single point on the focal plane, into a potentially large locus. This can affect many different types of measurements, particularly feature photometry (e.g., DeForest et al. 2009). It is possible to infer instrument PSFs from science images, especially if the image sequence includes bright point-like features such as solar flares and/or occulting bodies such as the Moon. The inferred PSF can then be used to reduce the effect of convolution on the image—a process called “known-PSF deconvolution.”

Deconvolution is an art rather than a precise science because it is an ill-posed problem. The set of all images forms a semigroup under convolution: for any PSF it is possible to construct an *approximate inverse* PSF that approximately cancels its effect. For real instrument PSFs, these inverses typically amplify high spatial frequencies, increasing the noise level of the corrected image. The noise can overwhelm the image in common cases. This effect is overcome by simple filtering (e.g., Wiener filtering; Press et al. 2007) or by Bayesian iterative techniques, such as the Richardson–Lucy method (Prato et al. 2012). Blind

deconvolution (systematically trying different possible PSFs and assessing whether the image has improved, iteratively or non-iteratively) can be used to infer both a PSF and an image from a single data set, but is “fraught with peril” (Claerbout 1990). In the present work, we carried out the deconvolution by direct approximate inversion of the measured PSF, with a Wiener filter to regularize the inverses (see DeForest et al. 2009 for details of the technique). The telescope images can be convolved directly with these derived inverse PSFs to yield a corrected image.

Grigis et al. (2011) have obtained the PSFs for all the Atmospheric Imaging Assembly (AIA) channels. A direct comparison of our PSFs with those of Grigis et al. (2011) is beyond the scope of the present paper. However, we point out the major differences between the method adopted by Grigis et al. (2011) and our present analysis. (1) The core of their PSFs accounts for effects such as instrument jitter, CCD pixelization, charge spreading, and scattering by the primary and secondary mirrors. The core width is determined by root mean square spot diameter using pre-flight estimates of the telescope focal performance (see Grigis et al. 2011 for details). In our present paper, we set the core of our model PSF as 0.2 pixels; this is because we were interested in characterizing the stray-light performance rather than sharpening the image. (2) In Grigis et al. (2011), the PSFs consist of a Gaussian core and a mesh diffraction pattern, but we have an additional component that deals with the diffuse scattering represented by the sum of a Gaussian truncated Lorentzian and a shoulder Gaussian. (3) Grigis et al. (2011) consider the diffraction effects from the meshes supporting both the entrance filter and the focal plane filter when modeling the PSFs whereas, in this paper, we

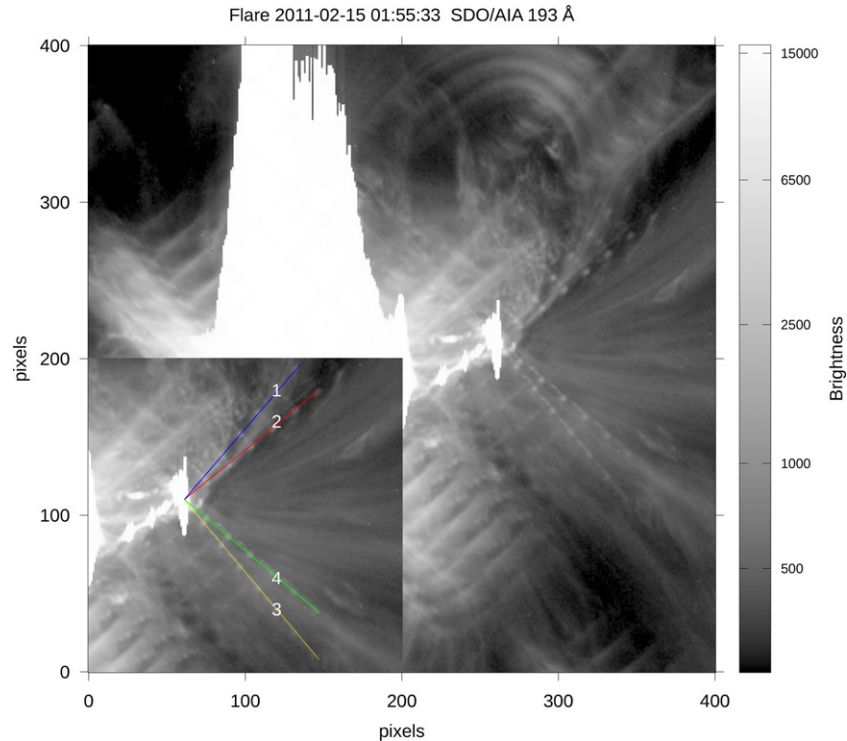


Figure 1. Diffraction pattern caused by the mesh supporting the entrance-filter in the *SDO/AIA* channels. This image was taken in 193 Å at 01:55:33 UT on 2011 February 15. Orders well beyond six are visible. Since the main flare caused CCD saturation, we selected a nearby subflare (shown in the inset). The four lines labeled 1–4 are the four diffraction arms used for constructing the diffraction pattern (the diffraction kernel in Equation (1)). (A color version of this figure is available in the online journal.)

consider only the diffraction caused by the entrance filter mesh. This is because the diffraction effects caused the focal plane filter can be removed by flat-fielding (Boerner et al. 2012; Lemen et al. 2012). The measurement of diffraction pattern in Grigis et al. (2011) is similar to that presented here and the spacings and orientations obtained agree with each other.

We report on modeling and computation of the PSFs and their inverses for all the seven EUV channels of the AIA telescope on board the *Solar Dynamics Observatory (SDO)*. In Section 2 we describe the AIA instrument, the data, and the main features of the PSFs observed in the AIA data. Section 3 describes the PSF we modeled. The method we adopted to infer the PSFs from images of solar flares and the lunar occultation are described in Section 4. We present our results in Section 5 and discuss the PSF characterization, the limitations (Section 5.1) of the technique we employed, and how to identify artifacts that are caused or highlighted by the application of PSFs. In Section 6, we demonstrate the usefulness of our PSFs in improving the AIA images and their influence on differential emission measure (DEM) analysis. We conclude by summarizing the PSF characteristics and their implications for the analysis and interpretation of the AIA data in Section 7.

An online supplemental file contains the PSFs and their inverses in FITS form suitable for direct application to AIA data.

2. INSTRUMENT AND DATA

The AIA telescope array on board *SDO* (Pesnell et al. 2012) takes full-disk solar images in seven EUV wavelengths, two FUV wavelengths and one in visible light (Boerner et al. 2012; Lemen et al. 2012). AIA consists of four 20 cm, dual-channel, normal-incidence telescopes with a field of view of 41', pixel size of 0".6 (12 μm), a spatial resolution of 1".5, a

10–12 s temporal resolution and 4096 × 4096 pixel CCDs. Two filters—one situated at the telescope aperture (the entrance-filter) and the other (focal-plane filter) located in front of the focal plane—block off-band light. The wavelength of interest is selected by narrow-passband multilayer mirrors (e.g., Walker et al. 1990) for the three EUV telescopes. The fourth telescope views FUV and contains a selector mechanism to choose the wavelength. The filters are mounted on a square mesh with a spacing of 360 μm. The mesh-bars are 29–33 μm thick. The mesh supporting the focal-plane filter produces a faint shadow in the focal plane that can be removed by flat fielding (Boerner et al. 2012; Lemen et al. 2012). The mesh supporting the entrance-filter acts as a two-dimensional grating with a square opening (Hecht & Zajac 1979; Lin et al. 2001; Gburek et al. 2006) and causes Fraunhofer diffraction of the incoming EUV light. The mesh consists of two segments with orientations 40° and 50° relative to the focal plane, giving rise to a distinguishable eight-armed diffraction pattern that is best seen in high-contrast images as in the case of solar flares (Figure 1). The diffraction pattern varies with the wavelength of the incoming light, the thickness of the mesh-bars and the spacing between them, and the orientation of the mesh segments with respect to the focal plane.

We used the Level 1 AIA data available for download from the Joint Science Operation Center (JSOC: <http://jsoc.stanford.edu/ajax/lookdata.html>) for all the EUV wavelengths—94, 131, 171, 193, 211, 304, and 335 Å. The Level 1 data are processed from Level 0 data and are fully calibrated (Lemen et al. 2012). That is, the Level 1 data are corrected for “overscan” rows and columns, dark currents removed and flat-fielded, have bad-pixels replaced by interpolated values and are despiked, are flipped to have the north pole at the top of each image, and have the metadata updated to include the instrument roll angle, the camera gain, the effective area, and the

alignment information (see Lemen et al. 2012; Boerner et al. 2012 for details). Some artifacts remain (e.g., Figure 9). The Level 1 data are 32-bit floating point numbers.

3. MODEL PSF

We modeled each telescope's PSF semi-empirically by fitting two components: a directly measured diffraction kernel; and a fitted, isotropic scattering profile similar to that used by DeForest et al. (2009). Mathematically,

$$\text{PSF} = e^{-4 \ln(2)r^2/\sigma^2} + D(r, \theta) + \alpha \frac{e^{-4 \ln(2)r^2/\sigma_r^2}}{(r^2\omega^{-2}) + 1} + \beta e^{-4 \ln(2)r^2/\sigma_s^2} \quad (1)$$

where r is distance in the image plane, $D(r, \theta)$ the diffraction pattern discussed below, α and β the relative strengths of the Lorentzian wings and the Gaussian shoulder, respectively, ω the width of the Lorentzian, and σ , σ_r , and σ_s the FWHMs of the central core of the PSF, the truncating Gaussian, and the shoulder Gaussian, respectively.

Besides diffraction and stray light, a typical AIA image is likely to contain other types of artifacts such as CCD overflow or saturation and the vertical stripes seen in the middle panels in Figure 9. These types of effects cannot be described by a simple convolution, and therefore, deconvolution of the AIA image with our PSF will not remove or reduce the effects of such artifacts.

3.1. Diffraction

From the theory of Fraunhofer diffraction (e.g., Hecht & Zajac 1979), in the case of ideal, uniformly spaced obstructions, the distance d_m of the principal maxima of the diffraction pattern from the center (or zeroth order) can be calculated using the relation:

$$d(m) = m \frac{\lambda}{a} \quad (2)$$

where m is the diffraction order, λ the wavelength of the light used, and a the distance between the mesh bars. Further, the intensity of the zeroth order of the diffraction pattern is related to that of higher orders $m = 0, 1, 2, \dots$ via a sinc function envelope:

$$I_0 = I_m \left(\frac{\sin(m\pi b/a)}{m\pi b/a} \right)^{-2} \quad (3)$$

where I_0 and I_m are the intensities of diffraction orders zero, and m and b are the width of the square-mesh openings. The filters used in *SDO/AIA* are similar to those used in the *Transition Region And Coronal Explorer (TRACE)* telescope. Lin et al. (2001) and Gburek et al. (2006) have carried out detailed analyses of the diffraction pattern observed in the *TRACE* images.

3.2. Isotropic Scatter

In addition to the diffraction pattern, the AIA images show evidence of a smoother, extended scattering profile in the form of the diffuse brightness seen in Figure 2. Adopting the technique of DeForest et al. (2009), modified for *SDO/AIA*, we modeled the scatter with an isotropic parametric shape and fitted it iteratively. The scattering profile we modeled is the sum of a narrow core, a truncated Lorentzian, and a Gaussian shoulder. The model PSF given in Equation (1) is computed by obtaining the best-fit values for all the parameters, except for σ , using the well-known amoeba algorithm (Press et al. 2007).

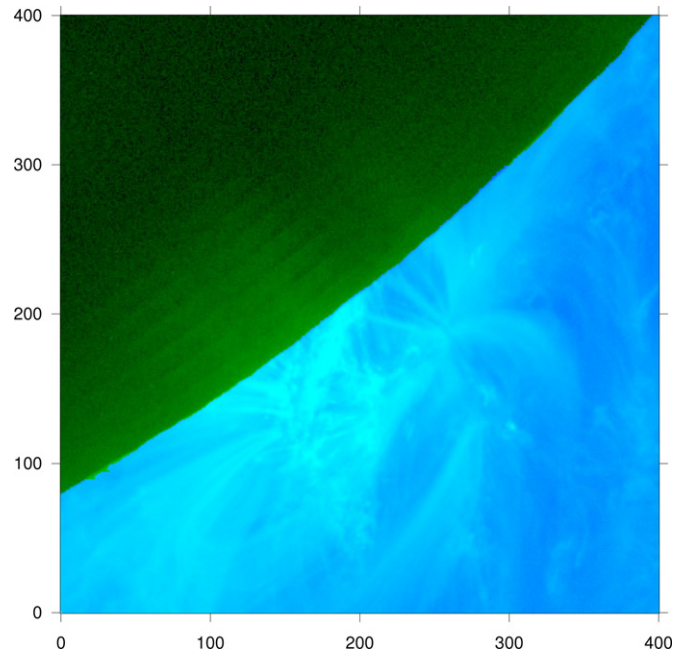


Figure 2. Identifying the Moon: pixels identified as lunar have yellow hue; those identified as solar are shaded blue to white. The faint ridges in the moon are the effects of diffraction caused by the mesh supporting the entrance filters in the *SDO/AIA* telescopes.

(A color version of this figure is available in the online journal.)

3.3. Inverse PSFs and Wiener Filter

Deconvolution with PSF is known to increase the noise (which is, in general, a combination of additive uncorrelated noise, multiplicative uncorrelated noise, and calibration error) in the image. Wiener filter (Press et al. 1989) deals with the optimal balance between signal amplification and noise suppression. Instead of developing the ideal Wiener filter for each image, we used a reciprocal that rolls over after a certain level of amplification to prevent excessive noise amplification and is adequate for a range of noise levels:

$$\Re_{\alpha, \epsilon} = \left(\frac{z^*}{|z|} \right) \frac{|z|^\alpha}{|z|^{\alpha+1} + \epsilon^{\alpha+1}}, \quad (4)$$

where $|z|$ is complex but α and ϵ are real. $\Re_{\alpha, \epsilon}$ converges to z^{-1} for large values of z and to $z^* |z|^{\alpha-1} \epsilon^{-\alpha-1}$ for small values of $|z|$ (when compared with ϵ), and rises to a maximum value close to $\alpha \epsilon^{-1}$.

4. METHOD OF ANALYSIS AND SELECTION OF DATA

Direct extraction of a complete PSF from a collection of scientific images is notoriously difficult. However, the overall effect of the PSF can be well characterized inside the lunar limb (planetary disk) during lunar (planetary) occultations of the Sun, while the diffraction effects caused by the mesh supporting the entrance filter can be measured directly from the pattern visible around bright point-like sources such as solar flares. In the present work, we derived our model PSF for each AIA telescope in two steps: (1) construction of the diffraction pattern by directly measuring the geometry and the principal maxima of the diffraction pattern observed in flare images; (2) fitting the diffuse components using a forward-modeling fit process operating on lunar eclipse images containing the lunar limb. These steps are further elaborated in the coming sections.

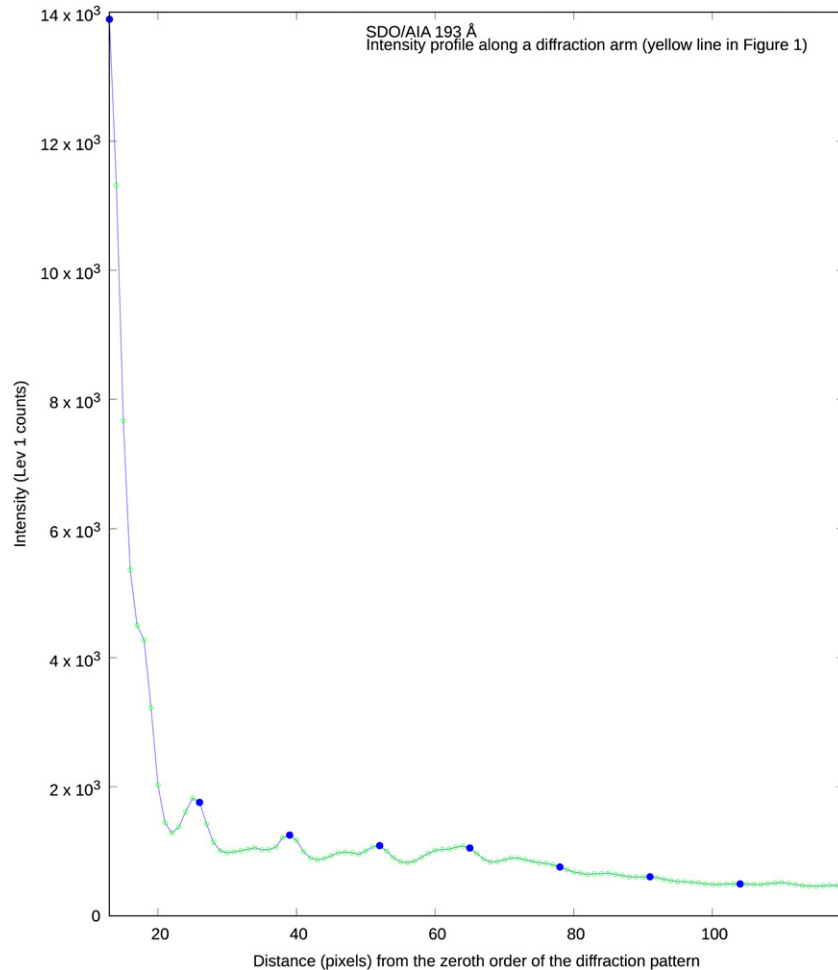


Figure 3. Intensity profile along the diffraction arm marked by yellow line in Figure 1 for 193 Å. The first solid (blue in the online color version) circle represents the center (zeroth order) of the diffraction pattern and the subsequent ones are the measured centers of each bright spot or the principal maxima. They are roughly 13 pixels apart. The small, open (green in the online color version) circles indicate each pixel.

(A color version of this figure is available in the online journal.)

4.1. Selection of Flare and Lunar Occultation Data

Flare images. Figure 1 presents the flare of 2011 February 15, caused by the sunspot group 1158. This *SDO/AIA* image was taken in 193 Å wavelength at 01:55:33 UT. The diffraction pattern caused by the entrance-filter in the AIA telescope is clearly visible in this image. However, strong flares cause CCD saturation of the flaring area, seen as the bright patch in the center of Figure 1. This in turn obscures the first few orders of the diffraction pattern, including the zeroth. On the other hand, if the flare is weak, the diffraction pattern blends with the background and the diffraction orders become indistinguishable. Therefore, finding AIA images displaying distinguishable diffraction pattern with the first few orders clearly identifiable and the zeroth order not going to saturation was a challenge. We found that the small flaring area (marked by colored lines in Figure 1) close to the main flare satisfied these criteria. The X2-class flare peaked at 01:56 UT. We selected images between the hours 01:55:00 and 01:55:52 UT.

Lunar occultation images. *SDO/AIA* observed the lunar transit on several occasions, but during the 2011 March 4 transit the instrument’s image stabilization system (ISS) was kept on (P. Boerner 2012, private communication). As a result, in those images there was little or no blurring of the images even well after the first contact of the moon. We selected images

between 13:00:01 and 13:04:05 UT. This transit, the green area in Figure 2, clearly exhibits the effects of stray light as diffuse brightness inside the lunar disk and the diffraction effects as dark and bright ridges near the active region.

4.2. Modeling the Diffraction Pattern

Figure 1 shows the eight-armed diffraction pattern caused by the mesh supporting the entrance filter. Here, orders up to 20 and beyond are identifiable without ambiguity. However, we used only the first six to seven maxima in all the EUV wavelengths for the present study, since that was sufficient to construct the diffraction pattern. The centers of the bright spots along each arm are the principal maxima of the diffraction orders. The centers of the bright spots were initially determined by eye. In order to model the diffraction, we needed the orientations of the arms and the spacings between the principal maxima (i.e., the geometry of the pattern) and the intensities of the principal maxima above the background.

Geometry of the pattern. We noted the angle through which each arm was rotated to make it parallel to the *X*-axis as the orientation. We determined the core—the zeroth order—of the diffraction pattern as the point of intersection of the four colored lines overlain the diffraction arms in Figure 1 and measured the coordinates of this point. We obtained the spacings between the

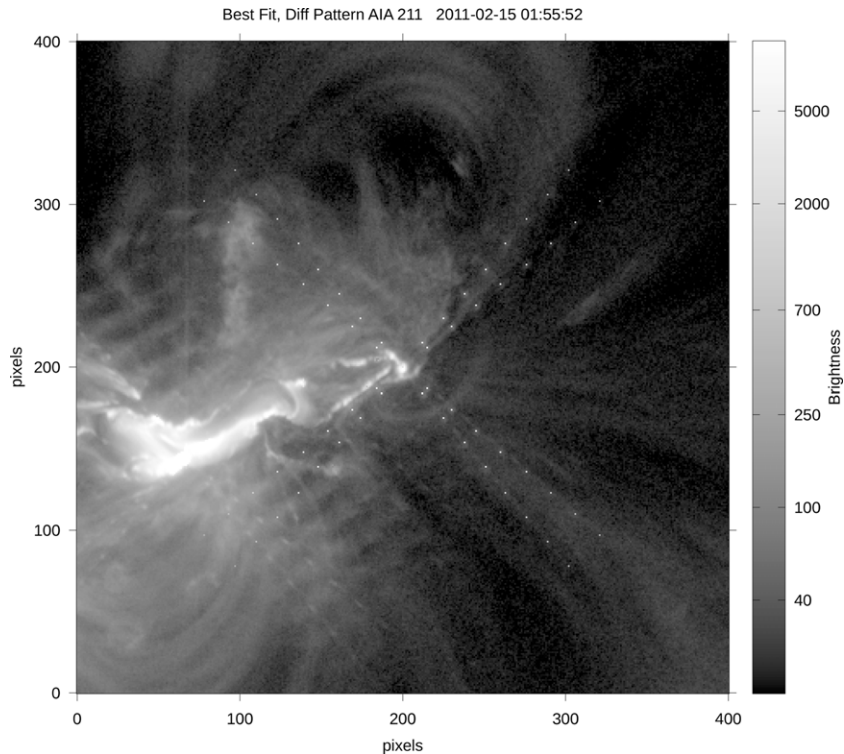


Figure 4. Fitted diffraction pattern overlain the original image. This *SDO/AIA* image was taken in 211 Å at 01:55:28 UT on 2011 February 15.

diffraction orders by measuring the coordinates of the principal maxima and calculating the distances between them for all four arms. We noted that the spacings for a given wavelength were not uniform but differed by 1–2 pixels.

Zeroth order intensity. Figure 3 shows the intensity profile along a diffraction arm. Here, the first solid circle corresponds to the center—the zeroth order—of the diffraction pattern and the subsequent ones represent the principal maxima of higher orders. The green circles denote the pixels from the center of the diffraction pattern. The intensity at the center (the zeroth order) of the pattern was measured directly from the image. We noted that CCD saturation caused by the flare introduced considerable ambiguity in the measurement of the zeroth order (higher orders as well) intensity. In other words, the CCD pixels near bright image features (such as flares)—that cast the diffraction patterns—tend to saturate and bleed. This makes it difficult, or even impossible, to locate the lowest orders of the diffraction pattern and measure their brightness.

Intensities at higher orders. We found that the measured location of the principal maxima did not always coincide with the local maxima—the centers of the bright spots—in image brightness, but differed by 1–2 pixels (as in the case of spacings), contrary to expectation. We attribute these discrepancies to the presence of non-uniform background and photon noise in the bright spots, or to unknown distortion in the instrument related to flare response. Moreover, the CCD saturation of the core region adds additional background around higher orders. Therefore, instead of taking the direct image value at each of the bright spots (the solid circles in Figure 3) as the intensity of the principal maxima, we computed it the following way. We obtained the average intensity, I_{peak} , in a 3×3 (pixels) area around them. In a similar way, we calculated the average intensities of the troughs that preceded (I_{prec}) and succeeded (I_{succ}) a given bright spot, and subtracted their mean (I_{trough}) from I_{peak} to obtain the intensity at each principal maxima.

The spacings and orientations were optimized iteratively using the well-known algorithm *amoeba* (Press et al. 2007) with a least-squares difference heuristic against the intensities, and the diffraction pattern was constructed on an 801×801 pixel grid. We did the computation on a larger grid, 1201×1201 , but did not see any significant improvements in the results; 801 was sufficient to cover the observed effects.

Theoretical computations of intensities. As mentioned above, since CCD saturation near bright objects causes ambiguity in the determination of intensities at the lowest diffraction orders, we computed the intensities of the core and higher orders theoretically using Equation (3). We obtained a best-fit value for the factor b/a for each wavelength, (e.g., 0.892 for 211 Å channel; see Lin et al. 2001 for a detailed discussion of the computation of b/a). Then, using the measured values of higher order intensities, we computed the average zeroth order intensity. Using this value, and Equation (3), modified, we computed all the higher order intensities.

We found that the measured intensities were significantly different from the computed values, and that the theoretical diffraction pattern better explained large-scale stray-light features such as the ridges in Figure 2 than the directly measured diffraction pattern. Therefore, the theoretically computed intensities were used to optimize the spacings and orientations, as discussed above, and obtain the diffraction kernel. We attribute the improvement to noise in each individual measurement, which is suppressed by averaging multiple measurements into a single-parameter fit. The fitted orientations and the spacings are presented in Table 1 and the fitted pattern overlain the original image in 211 Å is shown in Figure 4.

4.3. Fitting the Model PSF

We computed each PSF kernel iteratively on an 801×801 pixel grid with a pixel resolution of $0''.6$, and the parameters of Equation (1). We used the darkness in the occulting lunar

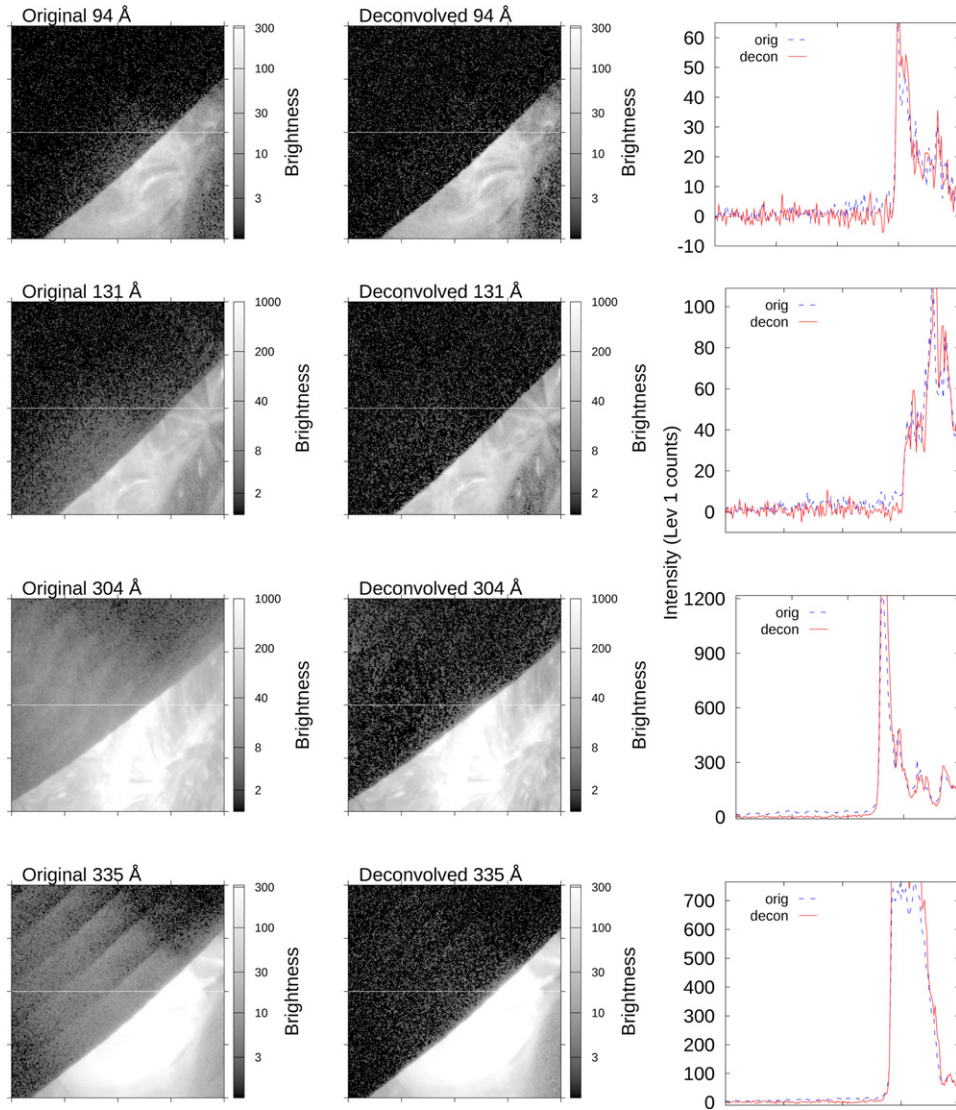


Figure 5. Comparison of the original (left panel) and deconvolved (middle panel) images for the *SDO/AIA* EUV channels, 94, 131, 304, and 335 Å, during the lunar transit on 2011 March 4. The right panels depict the intensity variations along a raster (white horizontal line in the left and middle panels) in the original (dashed) and the deconvolved images (solid line).

(A color version of this figure is available in the online journal.)

Table 1

The Spacings and the Orientations for Each Arm of the Diffraction Pattern

λ (Å)	Spacings				Angles			
	Arm 1	Arm 2	Arm 3	Arm 4	Arm 1	Arm 2	Arm 3	Arm 4
94	8.867	8.867	8.867	8.867	39.767	49.967	-39.833	-49.963
131	12.3567	12.3567	12.3567	12.3567	39.767	49.967	-39.833	-49.963
171	16.277	16.267	16.281	16.237	40.057	49.917	-39.733	-49.963
193	18.361	18.361	18.361	18.361	39.967	50.167	-39.833	-49.963
211	19.87	19.87	19.87	19.87	39.97	49.97	-39.93	-49.93
304	28.867	28.867	28.867	28.867	39.867	49.967	-40.233	-49.963
335	31.867	31.867	31.867	31.867	39.767	49.967	-39.833	-49.963

disc (known to be EUV-dark) to constrain the fitting procedure via a least-squares difference heuristic. For this, we generated a *reference* image as follows. We cut a small slice of the original image of 1201×1201 pixels around the active region where the effects of diffraction and stray light are clearly distinguishable. Then we determined the precise location of the lunar limb as the pixel where the EUV brightness dropped below 50% of the

average on the nearby bright side of the limb. With this fitted lunar limb (Figure 2), we created a mask of the same size with zeros within the lunar limb and ones elsewhere. We multiplied the mask with the original image slice to produce our reference image—zeros in the occulted region and the observed values of the original image everywhere else. Starting with a set of initial guess values, we obtained a trial PSF. The reference image was convolved with the trial PSF to get a *test* image.

To optimize the PSF fitting, we formulated a heuristic that minimizes the RMS difference between the values inside the occulted region of the original lunar occulted image and the test image. We tried to penalize overcompensation more than undercompensation initially, but we realized that this was not necessary for the fit to converge. The best-fit values obtained for all the parameters in Equation (1) were used to compute the final PSFs and their inverses.

5. RESULTS AND DISCUSSION

Figures 5 and 6 show the quality of the fitted PSFs for all the seven EUV channels of *SDO/AIA* telescopes. The left and

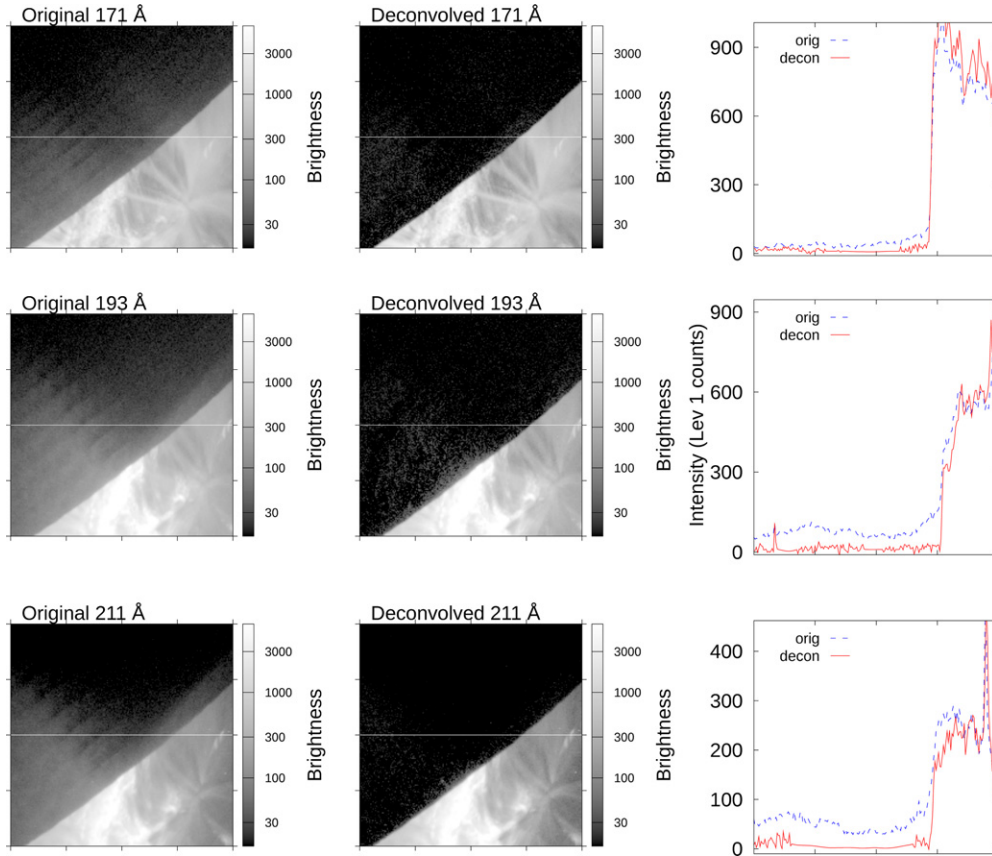


Figure 6. Same as 5 but for wavelengths 171, 193, and 211 Å.
(A color version of this figure is available in the online journal.)

middle panels show the original and deconvolved *SDO/AIA* images. The right panels represent the intensity variations along a particular raster (the white, solid lines in the left and middle panels) in the original (dashed line) and deconvolved (solid line) images. Ideally, the corrected or deconvolved images should look like the reference image, with zeros in the occulted region. The aim of the fitting procedure is to attain a corrected image as close to this as possible. We also checked for overcompensation in the deconvolved images. In a perfect fit, 50% of the pixels would be driven negative inside the lunar disk due to measurement noise around zero. In the actual fitted results, we noticed much less overcorrection than this, indicating that the fits are not overcompensating for scatter. The fitting was repeated for different sets of initial guesses of the parameters until a satisfactory deconvolved lunar interior, such as the ones presented in Figures 5 and 6, were obtained.

Our *ansatz* that the extended, non-diffraction scatter is isotropic is justified by the fact that the lunar profiles are well fitted by the resulting PSFs made by summing the measured anisotropic diffraction pattern and our isotropic scattering model. If there were additional anisotropic elements to the scattering, they would produce directional artifacts in the residual images in the vicinity of localized bright sources such as the active region in Figures 5 and 6. However, we do not see large directional swaths of residual brightness inside the corrected lunar image, indicating that our model adequately describes the functional form of the scattered light within the instrument.

The best-fit values of all the parameters in Equation (1) are given in Table 2. The FWHM (σ in Equation (1)) of the core was constrained to be 0.2 pixels (0.12 arcsec) since we were

Table 2
The Best-fit Values of the Parameters of Equation (1)
Obtained Using the Amoeba Algorithm

λ (Å)	α	ω (pixels)	σ_r (pixels)	β	σ_s (pixels)
94	1.256e-3	2.1	798	3.0e-2	1.721
131	2.0e-2	0.5	798	1.0e-3	2.6
171	1.76265	0.10122	798	1.2e-1	1.35
193	4.0e-4	3.9	798	8.0e-2	1.64
211	4.2e-4	3.6	798	2.35e-2	2.1
304	2.0e-2	0.2	798	1.0e-2	2.0
335	2.78e-4	1.90269	798	2.3678e-2	1.5924

interested in removing the effects of stray lights and diffraction rather than sharpening the image itself. We set the width of the truncating Gaussian (σ_r in Equation (1)) close to 800 pixels, the maximum possible with the selected grid size, so that the PSFs include scattering effects extending over a large region. We noted that σ_r was not influenced by *amoeba*, confirming that our choice was sufficiently broad. The relative strength of the Lorentzian is of the order of 10^{-2} – 10^{-4} for all wavelengths except for 171 Å where it is comparable to the amplitude of the shoulder Gaussian. This indicates that the shoulder of the 171 Å PSF is better fit by the Lorentzian than by the shoulder Gaussian term.

Figure 7 shows the best-fit PSF for wavelengths 193 and 304 Å, normalized to a total integral of unity. The maximum normalized intensity inside the core of the PSF varied between 0.70 (193 Å) and 0.81 (304 and 335 Å), and the contribution to the total energy from outside of a radius of $100''$ was insignificant.

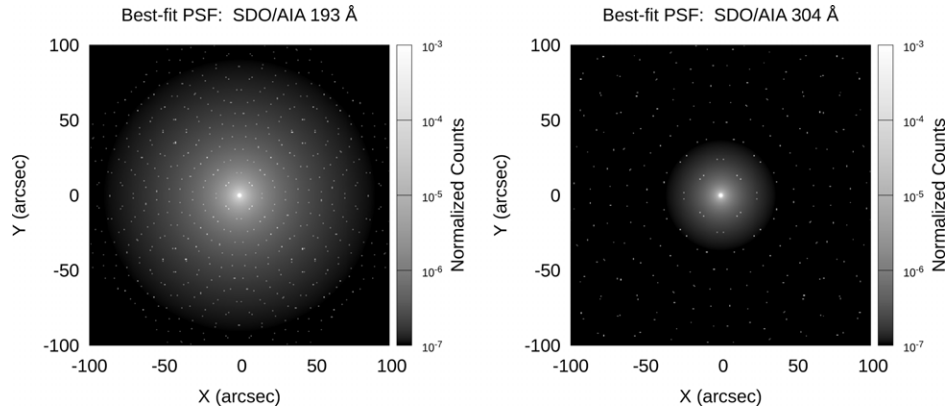


Figure 7. PSF computed for 171 and 304 Å, using Equation (1) and the best-fit parameters in Table 2. The PSFs are normalized to unity and are plotted on a log scale. The 171 Å image has the highest proportion of the isotropic scatter (compared to diffraction) among our measured PSFs while 304 Å has the lowest.

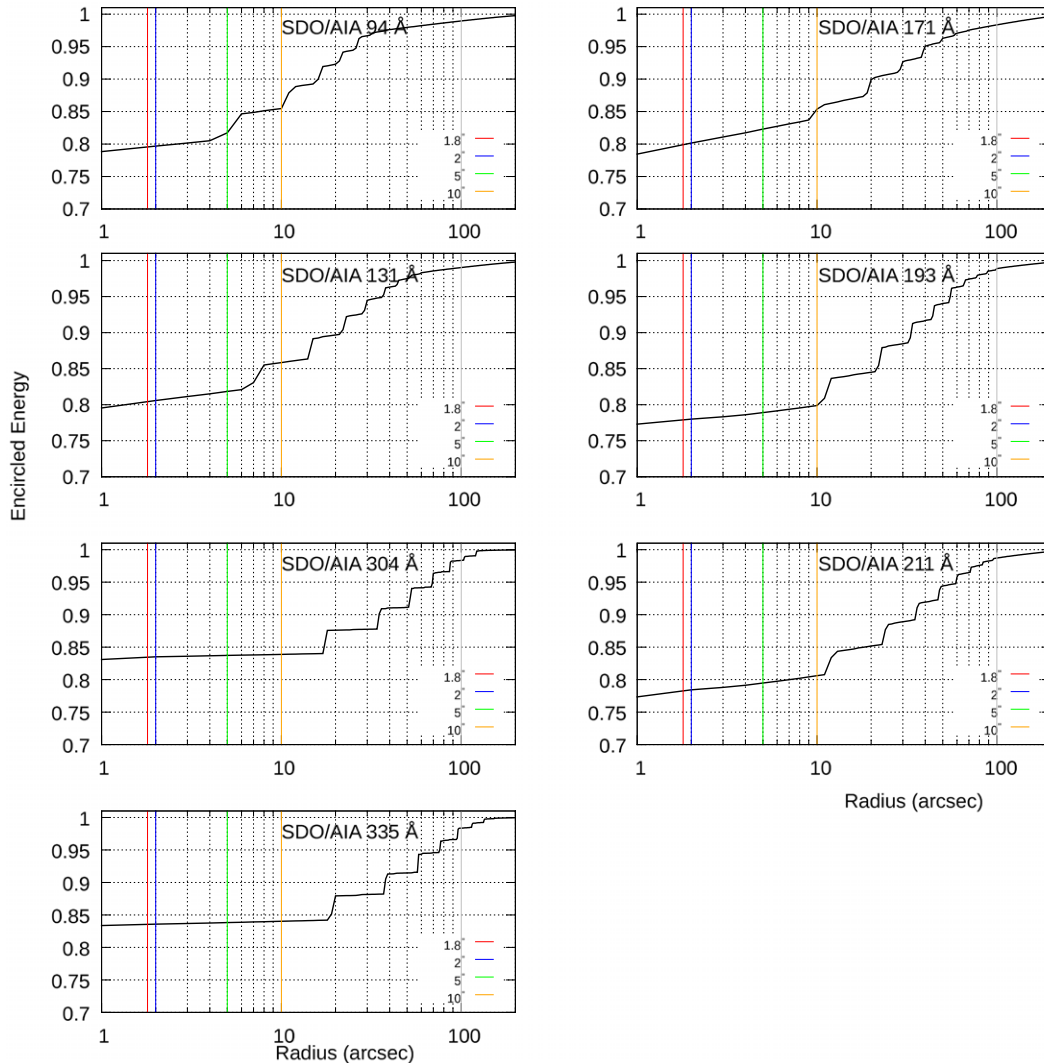


Figure 8. Encircled energy vs. distance plot for the PSF for all the EUV channels of *SDO/AIA*. The *Y*-intercept of each plot yields the entrance beam normalized scattering. (See the text for details.)

(A color version of this figure is available in the online journal.)

Encircled energy is an important measure of the type of stray light that is present in each telescope as it highlights the amount of extra illumination in each interior pixel of a bright, distributed image originating from elsewhere in the true (non-PSF-affected) focal plane. Figure 8 depicts the encircled energy versus distance for all the EUV wavelengths. Here, the vertical lines indicate

radii of 1.8'', 2'', 5'', and 10'', respectively. The plotted curves represent the total energy (normalized to unity) in the PSFs within a given radius. For example, the 94 Å plot at upper left shows that 79% of incident light into the AIA 94 Å channel arrives within 1'' of its intended location (diameter 2''), and, therefore, 21% of the incident light lands outside that distance.

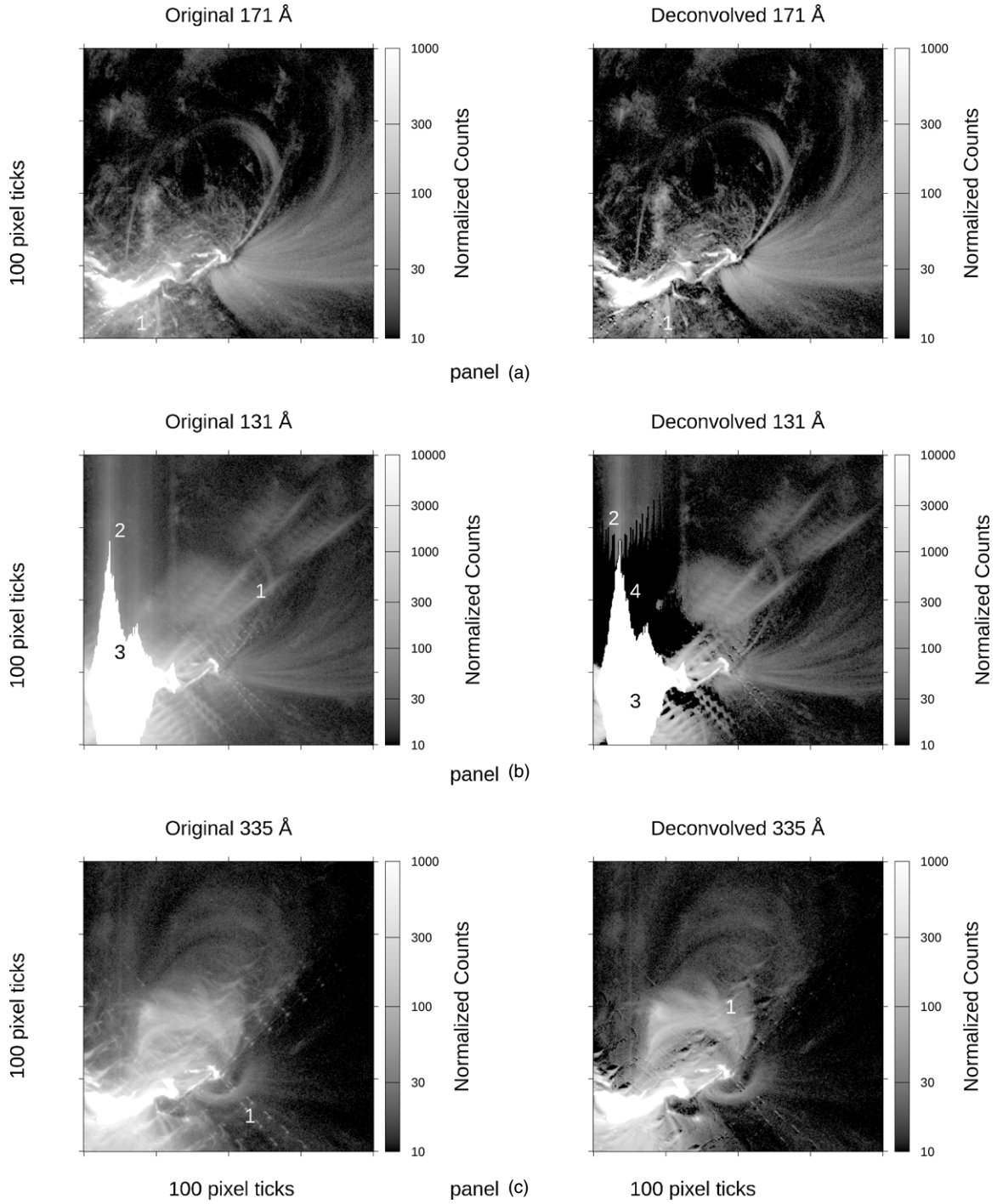


Figure 9. Flare of 2011 February 15, observed in 171 (top), 131 (middle), and 335 Å (bottom) wavelengths. The left panels depict the original images and the right panels the deconvolved images. This figure highlights the limits of image deconvolution. Note the residual detector errors (label 2) and saturation (label 3) effects in 131 Å and diffraction artifacts (label 1) due to the compact source in all the three channels. The diffraction pattern is seen as dark dots in the deconvolved images, a limitation of the deconvolution method. Label 4 in the deconvolved image in panel (b) indicates overcorrection due to CCD saturation and bleeding.

Further, 85% of incident light falls within $10''$ of the intended location, while 15% falls further away.

The nearly vertical steps in the encircled energy plots are due to the spiky diffraction pattern, and the sloping spaces between them are due to the smoothly modeled “scattering” portion of the PSF. The shape of the steps indicates the proportions of the stray light due to diffraction and other effects. For example, the 304 Å channel stray-light pattern is almost entirely due to the observable diffraction pattern, while the 94 Å channel has a higher proportion of smooth stray light from other effects.

The relative importance of the diffraction pattern varies among telescopes and is quantified in Table 3.

When analyzing image data from *SDO/AIA* telescopes, a more useful measure of scattered light is the image-normalized scatter: the ratio of stray light to non-stray light, normalized to the non-scattered brightness in the core of the PSF. This gives an estimate of the expected diffuse brightness in the image, given a measured brightness of well-focused features in the image. Table 4 summarizes the image-normalized scatter for all the EUV channels of the *SDO/AIA* telescopes. We have computed

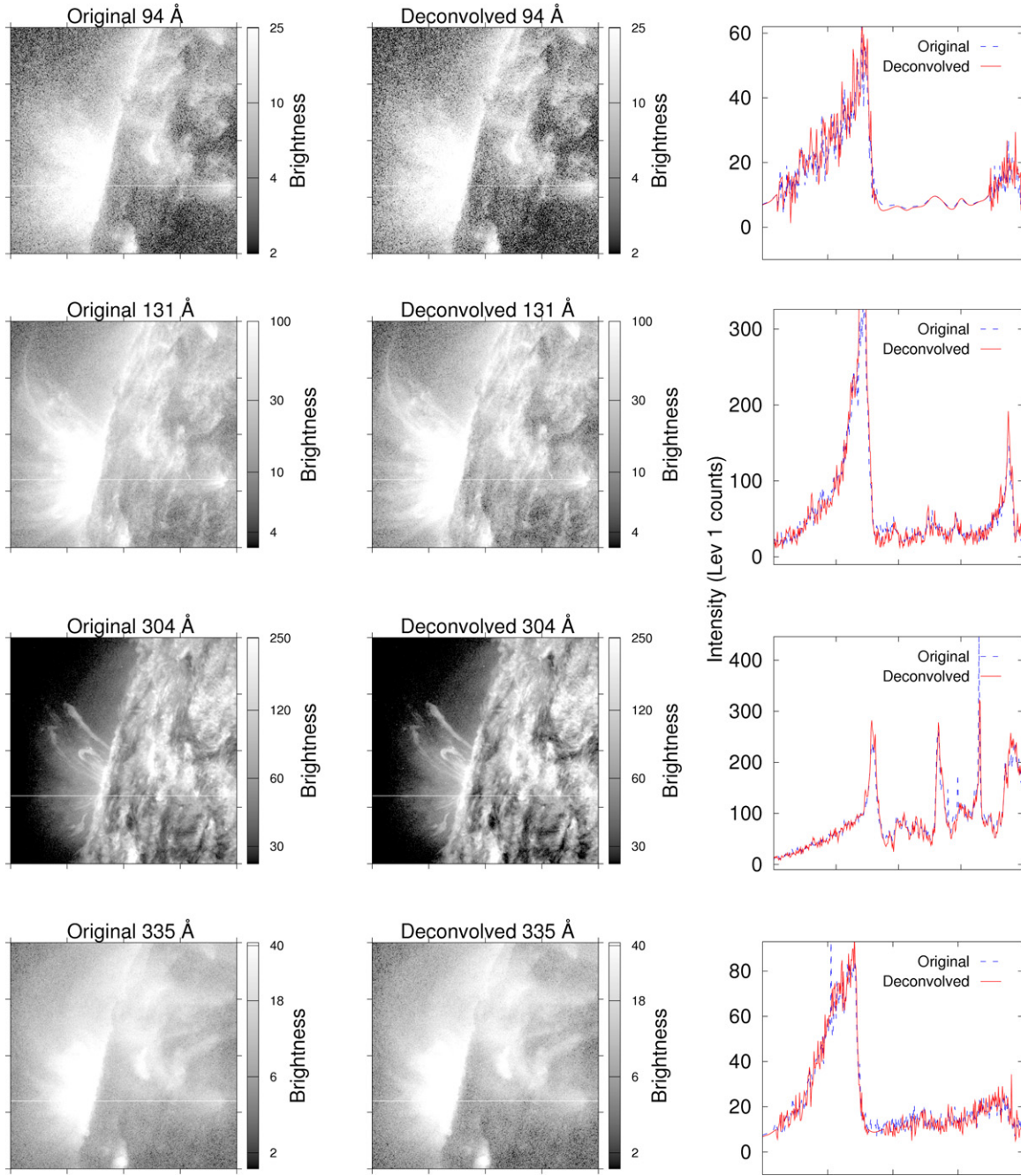


Figure 10. Application of the PSF: a coronal loop observed on the east limb on 2011 August 8 in 94, 131, 304, and 335 Å wavelengths, before (left panels) and after (middle panels) deconvolution with the respective PSFs. The right panels show the intensity variations along a particular raster (white horizontal lines in the left and middle panels) in the original (dashed) and deconvolved (solid) images.

(A color version of this figure is available in the online journal.)

the scatter at $2''.0$, $5''.0$, and $10''$ radii, normalized by that at a radius of $1''.8$, three times the resolution of *SDO/AIA*. We noted that the image-normalized scatter was the highest for 193 Å.

5.1. Limitations

Deconvolution techniques are far from perfect. The present analysis is limited in its scope to compensate for specific types of features in the images. In particular, the spiky diffraction pattern imposed by the entrance filter is difficult to remove for two reasons: (1) the spikes pose a difficult alignment problem during characterization of the PSF, and (2) it is not possible in theory to remove an occultation diffraction pattern by linear inversion.

The second point arises from basic Fourier optics: since the entrance filter is at a conjugate plane to the image, its PSF is its Fourier transform—hence the Fourier transformation step in the inversion reproduces an image of the opaque filter grid in silhouette. It is not possible to remove the grid from the Fourier plane by division because division by zero is not possible. In general, all objects are improved by deconvolution, whereas small, bright loci such as flare cores retain some diffraction-related artifacts.

Non-convolutional artifacts that can be found in the AIA images include a nonlinear response in the detector, per-row gain effects around moderately bright features, saturation and bleeding of very bright features, and flat-field artifacts. These

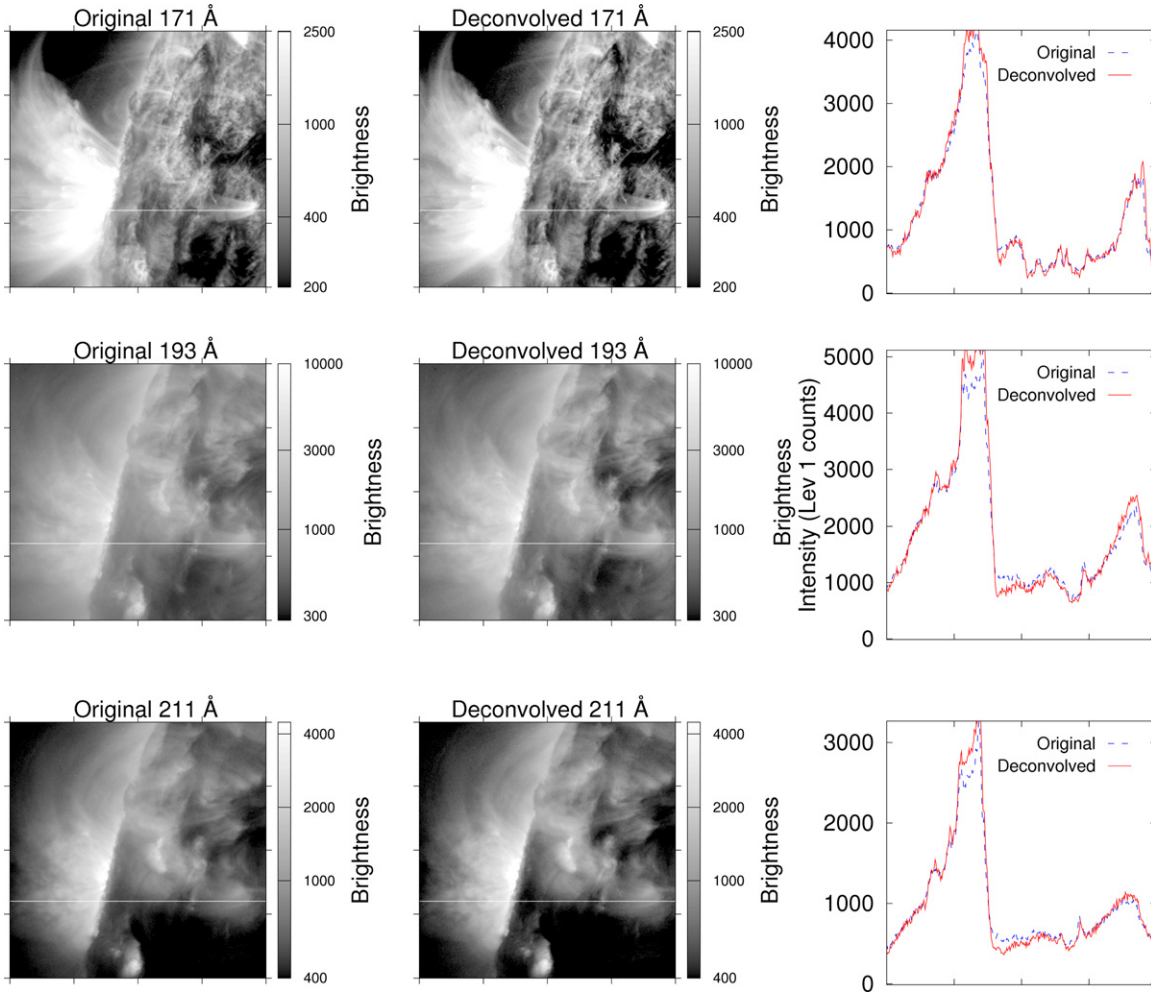


Figure 11. Same as 10 but for wavelengths 171, 193, and 211 Å.
(A color version of this figure is available in the online journal.)

Table 3
Percentage Contribution of Stray Light and Diffraction to the PSF
for All the EUV Channels of *SDO/AIA* Telescopes

λ (Å)	Percentage Contribution of	
	Stray Light	Diffraction
94	12	88
131	10	90
171	58	42
193	17	83
211	12	88
304	5	95
335	5	95

Table 4
The Image Normalized Scatter for All the EUV Channels
of *SDO/AIA* Telescopes

λ (Å)	Image Normalized Scatter		
	2''	5''	10''
94	27	25	19
131	26	23	18
304	20	20	19
335	20	19	19
171	27	23	20
193	29	28	26
211	29	27	25

Note. The image normalized scatter is the ratio of scattered to non-scattered light normalized by the scatter within a radius of 1''8 (see the text for details).

types of artifacts, when significant, are actually worsened by deconvolution because the effect is spread over a large portion of the image. They must be corrected by other means than simple deconvolution.

Figure 9 shows examples of a few of these limitations: (1) diffraction effects in panels (a), (b), and (c), are partially corrected by deconvolution (labeled as 1); (2) CCD artifacts, appearing as vertical lines, cannot be removed by deconvolution, (labeled as 2); (3) CCD saturation and bleeding of very bright features remain unaltered in the deconvolved images (labeled as 3); (4) overcorrection, the black regions seen in

the deconvolved image in panel (b), introduced by the deconvolution due to the CCD saturation and bleeding (labeled as 4).

6. APPLICATIONS

We used our PSFs to further demonstrate their usefulness and the effect of deconvolution on the stray-light characteristics by testing on two specific applications: (1) improvements of contrast and photometry, and (2) the DEM analysis.

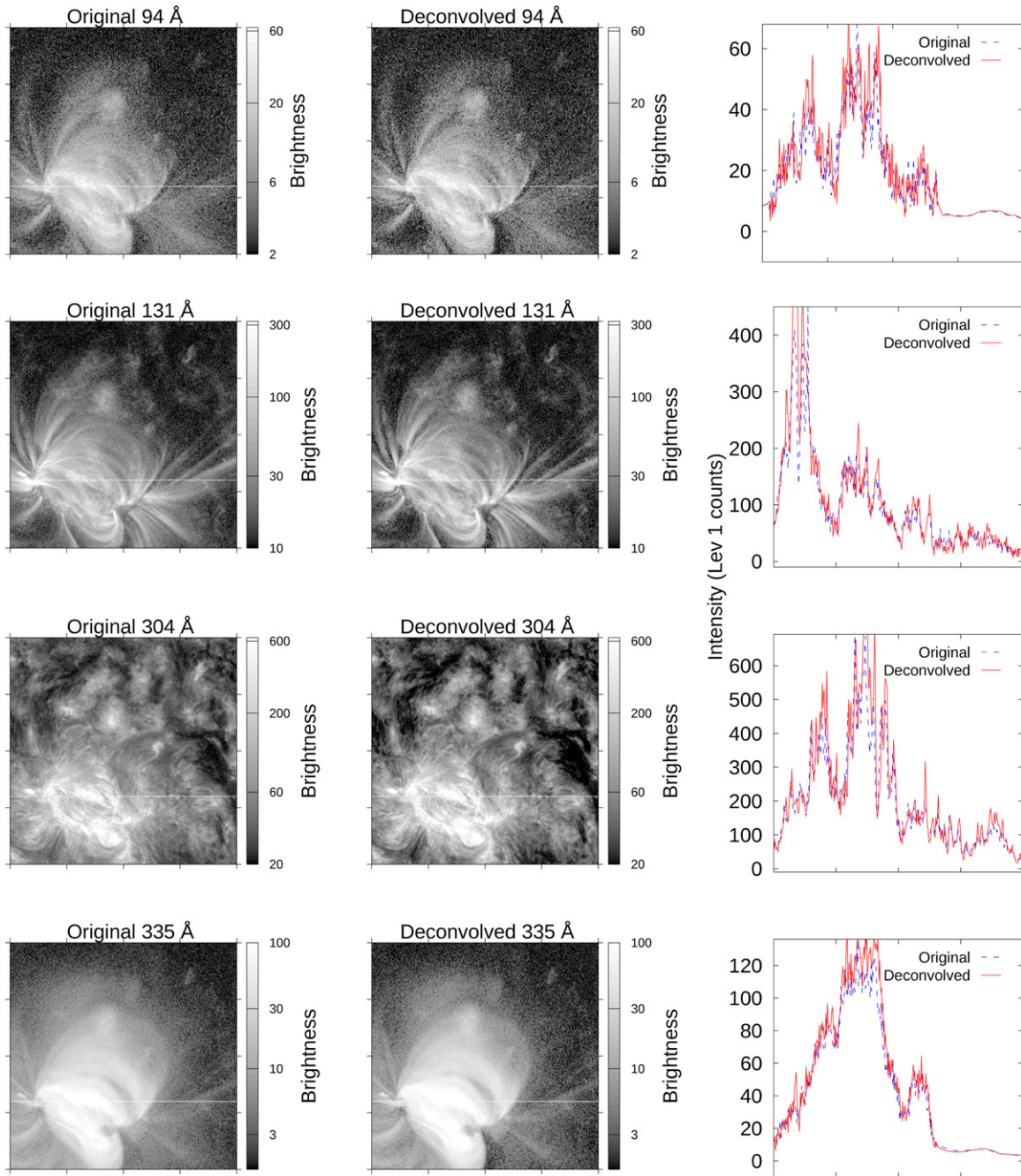


Figure 12. Same as Figure 10 but for a loop observed on the solar disk.
(A color version of this figure is available in the online journal.)

6.1. Contrast and Photometry Improvements

We selected two different features: (1) a coronal loop observed near the northeast limb and, (2) a loop near the disk center, from the 2011 August 8 data between the hours 08:05:09 and 08:05:19 UT, in all the EUV wavelengths, and deconvolved them using their respective PSFs. The results are shown in Figures 10–13. We plotted the original and deconvolved images in the left and middle panels, respectively. In the right panels, we plotted the intensity variations along a particular raster (marked by the white line) for the original (dashed lines) and deconvolved (solid lines) images. The intensities in the bright areas are larger after deconvolution while those in the dark areas are lower; an effect expected of the deconvolution process. The

effect is particularly pronounced in wavelengths 131 and 335 Å in Figure 10, in 171 Å in Figure 11, in 131 Å in Figure 12, and in 193 and 211 Å in Figure 13.

6.2. DEM Analysis of AIA Loops from Original and Deconvolved Images

DEM analysis is a technique used to study the structure of coronal loops and heating mechanisms, making use of solar observations in the UV, EUV, and X-ray wavelengths (e.g., Schmelz et al. 2010, 2013). DEM measurements are possibly contaminated by stray-light effects that mix nearby illumination into the loops under study. To understand the extent to which

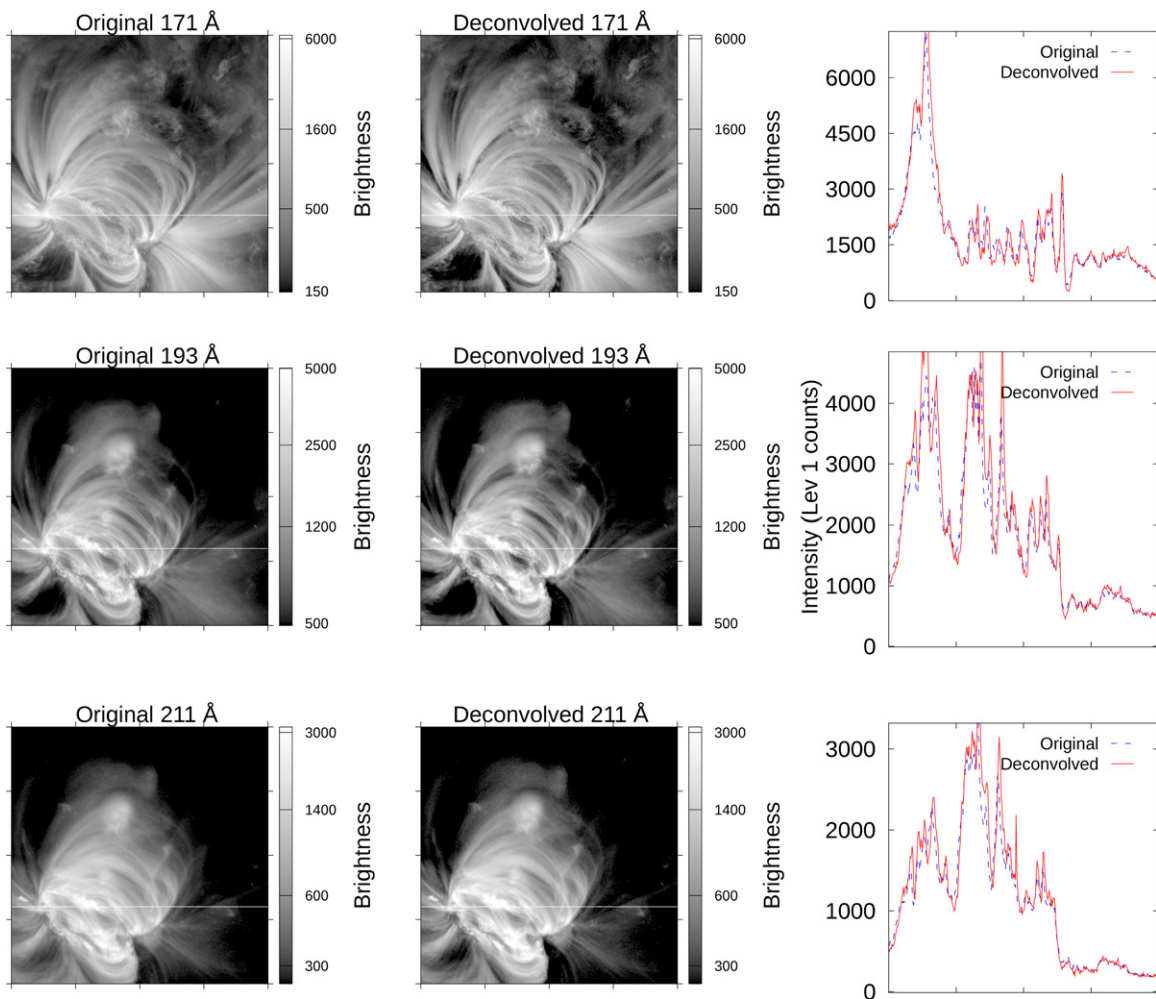


Figure 13. Same as Figure 12 but for wavelengths 171, 193, and 211 Å.
(A color version of this figure is available in the online journal.)

this contamination can affect the DEM measurements, we used the deconvolved *SDO/AIA* images for a comparative study.

We selected the coronal loops observed near the disk center on 2011 August 8 for the DEM analysis. We used the *SDO/AIA* images in all the EUV wavelengths except for 304 Å, which is not optically thin. Figure 14 shows the two coronal loops in 171 Å (labeled 1 and 2) we selected. The boxes on the left in 1 and 2 outline the loop segments, while the ones on the right show the background area. For both the original and the deconvolved data sets we (1) co-aligned the *SDO/AIA* images for the disk data sets; (2) selected a set of 10 pixels along the spine of a loop; (3) picked 10 nearby background pixels; (4) obtained the average and the standard deviations of the loop and the background pixels in each *SDO/AIA* image; (5) subtracted the average background and propagated the standard deviation errors; and (6) normalized the background-subtracted averages and uncertainties by the appropriate exposure times, resulting in units of Data Numbers per sec. For this analysis, we used the standard *AIA* response functions available in SolarSoft.

Figure 15 depicts the DEM results from the *xrt_dem_iterative2* routine that was originally developed by Weber et al. (2004) and tested by Schmelz et al. (2009) for XRT data alone. This routine, now applied more generally (Schmelz et al. 2010; Winebarger et al. 2011), uses a forward-fitting approach where a DEM is guessed and folded through each response to generate predicted

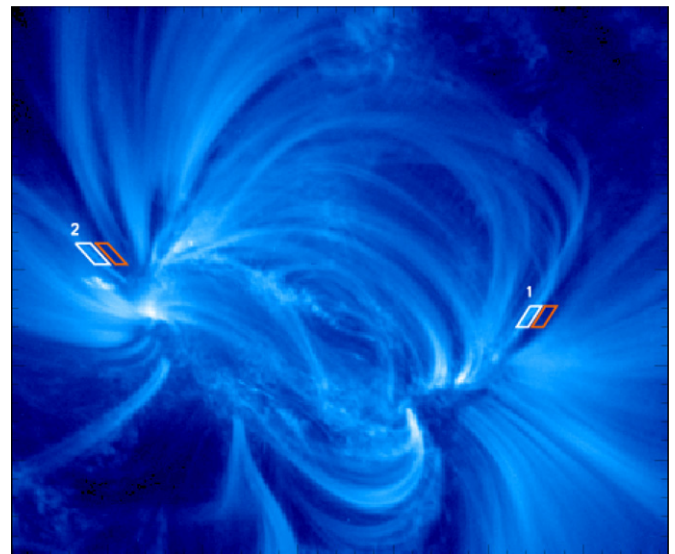


Figure 14. Labels 1 and 2 represent the two small sections of the coronal loops selected for the DEM analysis. This is an *SDO/AIA* image in 171 Å wavelength. The boxes on the left-hand side in both the Sections 1 and 2 outline the loop segments while those on the right show the background area.
(A color version of this figure is available in the online journal.)

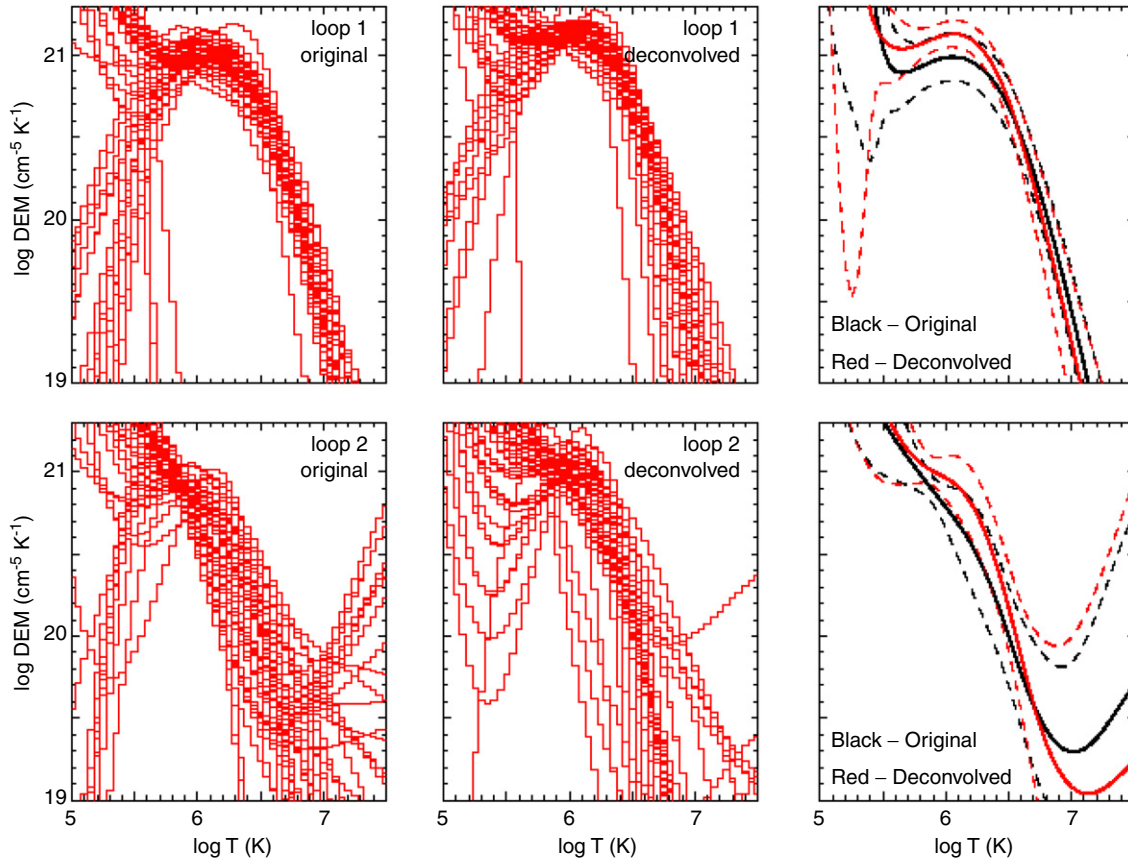


Figure 15. DEM results from *xrt_dem_iterative2* (Weber et al. 2004; Schmelz et al. 2009, 2010; Winebarger et al. 2011). The curves in the left and middle panels are 50 Monte Carlo realizations. In the right panels, we plotted the DEM means and variances calculated at each temperature for the original (black) and the deconvolved (red) images.

fluxes. This process is iterated to minimize χ^2 for the predicted-to-observed flux ratios. The DEM function is interpolated using several spline points which are directly manipulated by *mpfit.pro*, a well-known, much-tested IDL routine that performs a Levenberg–Marquardt least-squares minimization. There are $N_i - 1$ splines, representing the degrees of freedom for N_i observations. This routine uses Monte Carlo iterations to estimate errors on the DEM solution. For each iteration, the observed flux in each filter was varied randomly, and the program was run again with the new values. The distribution of these variations was Gaussian with a centroid equal to the observed flux and a width equal to the uncertainty.

The curves in the left and middle panels of Figure 15 are the 50 Monte Carlo realizations. We have treated the ensemble of Monte Carlo runs as a probability distribution at each ordinate value. We plotted in the right panels the DEM mean and variance calculated at each temperature, for the original (black) and deconvolved (red) data. The solid line is the mean and the dashed lines are the 1σ error curves. These results indicate that the two populations are similar, i.e., the solid curves are generally within 1σ of each other. This shows that the differences between the two plots are minor compared to the variation between different Monte Carlo trials. The analysis for both Loop 1 and Loop 2 shows that the deconvolution alone is not significantly affecting the DEM results.

7. CONCLUDING REMARKS

Optical telescopes convolve their images with a PSF that describes the response of the optical system to a point source,

resulting in the blurring of the images. The PSF typically includes core elements (not considered by us in this paper) that describe the focusing performance of telescope and broad elements that represent scattering of light in the telescope. The scattering component is rather difficult to measure in the lab because it combines very large area with very low intensity, but is easier to measure from occulted images in-flight. We determined the stray-light PSFs for all the EUV channels of the *SDO/AIA* telescopes semi-empirically and generated their inverses. The PSF we modeled (Equation (1)) consists of a diffraction kernel and an isotropic scattering term representing stray light. The inverse PSFs may be convolved directly with the respective Level 1 data to obtain the corrected (deconvolved) images.

Characterization of the stray-light PSF of each telescope yields insight into the quality and performance of its optical components. The best-fit PSFs for *SDO/AIA* vary from near-ideal to about twice worse than diffraction-alone PSFs. The worst telescope performs about twice as well as the *TRACE* instrument’s 171 Å channel did. We have demonstrated that the application of the PSFs improves the stray-light performance by a factor of upto 10 (Figures 5 and 6). Further, we showed that correction using the PSFs significantly improved contrast and the effect is more visible in dark features such as miniature coronal holes than in bright features (Figures 10–13). These findings emphasize that, as in the case of *TRACE* images, deconvolution improves the *SDO/AIA* images and reduces the global background “haze” significantly.

Moreover, we have carried out a preliminary analysis of DEM measurements using the deconvolved images. Our results

indicate that deconvolution alone does not affect DEM analysis of coronal loop segments when appropriate local background subtractions are used. We conclude that DEM results implying multithermality of coronal loops are not contaminated by PSF effects in AIA when properly background-subtracted. This result highlights that, although stray-light deconvolution is important for global background subtraction and photometry, especially in dark regions of an image, it is not necessarily required for differential brightness measurements of small features. If a suitable background element can be found sufficiently close to the feature under study, it is possible to generate suitable background-subtracted feature brightness.

All our PSFs and their inverses are available in the electronic digital supplement to this article, online at <http://psf.boulder.swri.edu>, and by e-mail to the authors. We provide the inverses for the convenience of the users as they may be applied to *SDO/AIA* images by direct convolution. The derived PSFs may prove useful for other types of regularized known-PSF deconvolution (e.g., Lucy–Richardson deconvolution or least-entropy methods).

We thank the *SDO/AIA* team for making the AIA data available via JSOC. We extend our gratitude to P. Boerner, D. Pesnell, R. Schwartz, and M. Cheung for helping us find eclipse images and for the many illuminating discussions. Thanks are also due to P. H. Scherrer for his help with exporting the AIA data from JSOC. Major part of the work was funded by the NASA SHP-GI program NNX09AG34G. Solar physics

research at the University of Memphis is supported by a Hinode subcontract from NASA/SAO as well as NSF ATM-0402729.

REFERENCES

- Boerner, P., Edwards, C., Lemen, J., et al. 2012, *SoPh*, **275**, 41
- Claerbout, J. F. 1990, *Geophysical Estimation by Examples* (Stanford, CA: Stanford Univ. Press) (http://sepwww.stanford.edu/sep/prof/gee/toc_html/)
- DeForest, C. E., Martens, P. C. H., & Wills-Davey, M. J. 2009, *ApJ*, **690**, 1264
- Gburek, S., Sylwester, J., & Martens, P. 2006, *SoPh*, **239**, 531
- Grigis, P., Su, Y., & Weber, M. 2011, AIA PSF Characterization and Image Deconvolution (<http://www.lmsal.com/sdodocs/>)
- Hecht, E., & Zajac, A. 1979, *Optics* (Reading, Mass: Addison-Wesley)
- Lemen, J. R., Title, A. M., Akin, D. J., et al. 2012, *SoPh*, **275**, 17
- Lin, A. C., Nightingale, R. W., & Tarbell, T. D. 2001, *SoPh*, **198**, 385
- Pesnell, D. W., Thompson, B. J., & Chamberlin, P. C. 2012, *SoPh*, **275**, 3
- Prato, M., Cavicchioli, R., Zanni, L., Boccacci, P., & Bertero, M. 2012, *A&A*, **539**, A133
- Press, W. H., Flannery, B. P., Teukolsky, S. A., & Vetterling, W. T. 1989, *Numerical Recipes* (Cambridge: Cambridge Univ. Press)
- Press, W. H., Teukolsky, S. A., Vetterling, W. T., & Flannery, B. P. 2007, *Numerical Recipes, The Art of Scientific Computing* (3rd ed.; Cambridge: Cambridge Univ. Press)
- Schmelz, J. T., Jenkins, B. S., & Kimble, J. A. 2013, *SoPh*
- Schmelz, J. T., Saar, S. H., DeLuca, E. E., et al. 2009, *ApJL*, **693**, L131
- Schmelz, J. T., Saar, S. H., Nasraoui, K., et al. 2010, *ApJ*, **723**, 1180
- Walker, A. B. C., Lindblom, J. F., Timothy, J. G., et al. 1990, *Optical Engineering*, Vol. 29, 581
- Weber, M. A., DeLuca, E. E., Golub, L., & Sette, A. L. 2004, in *IAU Symp. 223, Multi-Wavelength Investigations of Solar Activity*, ed. A. V. Stepanov, E. E. Benevolenskaya, & A. G. Kosovichev (Cambridge: Cambridge Univ. Press), 321
- Winebarger, A. R., Schmelz, J. T., Warren, H. P., Saar, S. H., & Kashyap, V. L. 2011, *ApJ*, **740**, 2